Modelling of Liquid Oxygen Two-Phase Flow Expansion at Sub- and Supercritical Pressure Conditions

Theodoros Lyras[1,*], Ioannis K. Karathanassis[1], Phoevos Koukouvinis[1], Manolis Gavaises[1]
[1]City, University of London, Northampton Square, London EC1V 0HB, United Kingdom
*Corresponding author: theodoros.lyras@city.ac.uk

Abstract
Liquid oxygen (LOX) constitutes a popular propellant used in multistage rockets for space launch vehicles. The delivery of LOX to mix with the main fuel can be realised at either supercritical (lower-stages of the tandem rocket structure) or subcritical (upper stages) pressure conditions. The present study demonstrates the applicability of different numerical approaches with regards to capturing phase-change of LOX in both sub- and supercritical regimes in a converging-diverging nozzle layout. Hydrodynamic-instability effects have been taken into account through unsteady Reynolds-averaged Navier Stokes (URANS) simulations and detached eddy simulations (DES). The phase-change rate between the compressible phases for subcritical, i.e. flash boiling, conditions has been predicted employing a kinetic theory of gases (Hertz-Knudsen) equation, whereas, for supercritical conditions the two-phase mixture properties have been obtained by look-up tables derived by the REFPROP dataset. The comparative investigation has demonstrated that the two-phase jet expansion dynamics exhibit much more profound features in the subcritical-pressure regime compared to supercritical expansion. DES has verified that the flow transition from supersonic to subsonic velocities at the edges of shock cells induces instabilities responsible for the formation of a transient secondary-flow pattern downstream the location of the Mach disk.

Keywords
Flash boiling; compressible flow; supersonic expansion; DES; shock diamonds

Introduction

Liquid oxygen (LOX) constitutes a widely used propellant in multistage rockets for space launch vehicles. The combination of liquid hydrogen/oxygen, as the fuel/oxidiser propellants mixture has been employed in various launch vehicles developed from the 1960s up to now [1]. Regardless of the fuel combination, LOX prevails as the oxidizer for most rocket engines. Lower stage engines operate within near-atmospheric conditions, whereas upper stage engines experience near-vacuum conditions especially during start-up. Depending on the stage of operation the delivery of LOX to the combustion chamber can be realised in super- or subcritical pressure conditions. For reference the critical point for oxygen corresponds to 50.4 bar/154.6 K [2]. Due to the pressure drop in the oxidizer delivery nozzle, LOX phase-change is expected. In the case that the process evolves at subcritical pressures, the fluid density exhibits an abrupt change as an interphase sets in between the liquid and gaseous phases. On the contrary, for supercritical conditions, no interface emerges and the liquid transits to the gas state in a continuous process.

There are relatively limited available experimental studies that focus on nozzle and spray flows of cryogenic oxygen. This is due to the technical challenges that cryogenic temperatures pose, especially at supercritical pressures [3]. The technical note of Hendricks et al. [4], available by NASA, reports measurements of the in-nozzle pressure distribution of a two-phase oxygen flow. Studies by Mayer and co-workers [5, 6] identified different topologies of cryogenic-liquid jets being discharged in sub- (of the order of 15 bar) or supercritical pressure conditions (100 bar). The backlit-illumination visualisation conducted by Chehroudi et al. [7] illustrated the topology of LOX and LN2 jets injected into a gaseous environment at conditions ranging from sub- to supercritical pressures and supercritical temperatures. Finally, the shadowgraphy visualisation of subcritical LOX and ethanol sprays conducted by Lamanna et al. [8] concluded that a higher degree of superheat is required for the inception of flash boiling in cryogenic compared to storable propellants.

Numerical studies on supercritical cryogenic-fluid injection are mainly focused on liquid nitrogen or oxygen as working medium. Zong et al. [9] performed an LES study referring to a LOX swirl injector using the SRK equation of state (EoS) for the calculation of the fluid thermodynamics. Kelvin–Helmholtz instabilities were demonstrated to be the primary cause leading to supercritical mixing. Wang et al. [10] employed the modified SRK EoS to describe the thermodynamic properties of LOX during supercritical injection, while in a subsequent study [11] the same approach was followed to illustrate the LOX/kerosene mixing characteristics. Referring to subcritical conditions, jet atomization and the formation of a two-phase spray is the process governing the combustion behaviour of the oxidizer/fuel mixture. Nevertheless, few numerical studies have been found in the open literature illustrating the distinct features of cryogenic-liquid flashing flow [12-15]. Lyras et al. [14] employed the Homogeneous Relaxation Model coupled to the volume of fluid method to predict the flashing phase-change in a throttle nozzle and

subsequent spray expansion of liquid nitrogen. Schmehl and Steelant [15] simulated in an Eulerian-Lagrangian frame the pre-flow of dinitrogen tetroxide (N2O4) oxidiser in a co-axial flow injector considering a dilute mixture of liquid droplets and vapour. An empirical model based on pre-existing measurements was used to describe the droplet flash vaporisation. A similar numerical approach was adopted by Ramcke et al. [16] to simulate the spray dynamics of LOX pre-flow and the mixing behaviour of the oxidiser with gaseous methane.
In this study, a comparative investigation on the predictive accuracy of different methods regarding in- and near-nozzle phase-change in both sub- and supercritical regimes is presented and a methodology based on the Helmholtz EoS applicable to both regimes is demonstrated. The present work focuses mainly on the in-nozzle, compressibility related, flow phenomena and elucidates their influence on the spray expansion and dynamics. Hydrodynamic-instability effects have been taken into account through URANS simulations and DES.

Numerical model

The geometrical configuration of the converging/diverging nozzle employed in this study is depicted in Fig. 1a and corresponds to the orifice used in the experimental investigation of Hendricks et al. [4]. An implicit pressure-based solver has been employed for both the URANS and DES simulations presented in this study. With regards to the URANS cases, a 5° three-dimensional axisymmetric wedge served as the computational domain. After a grid-independence study, an element count of 59800 was found as adequate to produce grid-independent results. On the contrary, the domain for DES comprised half of the actual geometry. The mesh element size was estimated based on the Taylor length scale equal to $\lambda_g = \sqrt{10}\, Re^{-0.5} L = 1.43 \times 10^{-5} m$ (where L is an indicative length scale taken equal to the throat diameter), which resulted to a computational grid of 4740960 elements having a topology depicted in Fig. 1b. The maximum CFL number throughout the domain was equal 0.94. A symmetry boundary conditions was placed to account for the domain truncation in both URANS simulations and DES. The rest of the basic boundary and initial conditions set for the cases examined, are summarised in Table 1.
The set of governing equations solved comprised the continuity, momentum and energy equations. Referring to the subcritical regime, a two-phase mixture approach was implemented including an additional equation for the vapour transport, as follows:

$$\frac{\partial(a\rho_v)}{\partial t} + \nabla(a\rho_v \vec{u}) = \dot{R}\,, \tag{1}$$

where the source term on the right hand-side of the equation corresponding to the phase-change rate has been modelled using the Hertz-Knudsen equation [17]:

$$\dot{R} = \frac{\lambda\, A_{int}\, (p_{sat} - p)}{\sqrt{2\,\pi\, R_g\, T_{int}}}\,, \tag{2}$$

where R_g is the ideal-gas constant and T_{int} is the bubble-interphase temperature. Since a mixture model is employed in this study, the interphase temperature is taken as equal to the local grid cell temperature provided by the solution of the energy equation. The total interphase area between the liquid and the gaseous phase A_{int} is calculated assuming a nucleation-site density of 10^{13} sites/m^3 and a bubble radius of 10^{-6} m [17]. The degree of deviation from thermodynamic-equilibrium is reflected on the value of the accommodation coefficient λ. A value of 1.0 has been set for the simulations corresponding to conditions similar to thermodynamic-equilibrium, which seems to provide the best fitting for experimental data available for water flashing flow in a converging-diverging nozzle. Both liquid/vapour phases were treated as compressible through the Tait and ideal-gas equations of state, respectively. On the contrary, a single-fluid approach was adopted for the simulations in the supercritical regime, where the fluid properties for each computational cell were provided by the REFPROP dataset. REFPROP provides tabulated values of LOX thermodynamic properties (e.g. density, enthalpy and speed of sound) calculated using an extended Benedict–Webb–Rubin EoS [18] and transport properties (viscosity and thermal conductivity) using the equations of state reported in [19].
Turbulence closure is required for all the cases examined, as the Reynolds number obtains values in the range 6 to 17×10^5. Referring to the URANS simulations, turbulence closure was accomplished with use of the k-ω SST model, which was also employed for the RANS section of DES. Numerical schemes with 2nd-order accuracy were employed for the discretisation of the governing equations. The bounded central differencing and QUICK methods were employed for the discretisation of the momentum and vapour-fraction equations respectively, while a second-order upwind scheme was used for density interpolation and turbulence transport equations. An implicit second-order backward differencing technique was used for time integration with a time step value of 10^{-6} s, resulting to a CFL criterion value less than 4 in the entire domain. Especially for the DES approach, a body force weighted scheme was used for pressure, while the bounded second-order implicit scheme was employed for time discretization with a time-step of $1\cdot10^{-7}$ s resulting to a maximum value of CFL criterion of 0.94 throughout the domain.

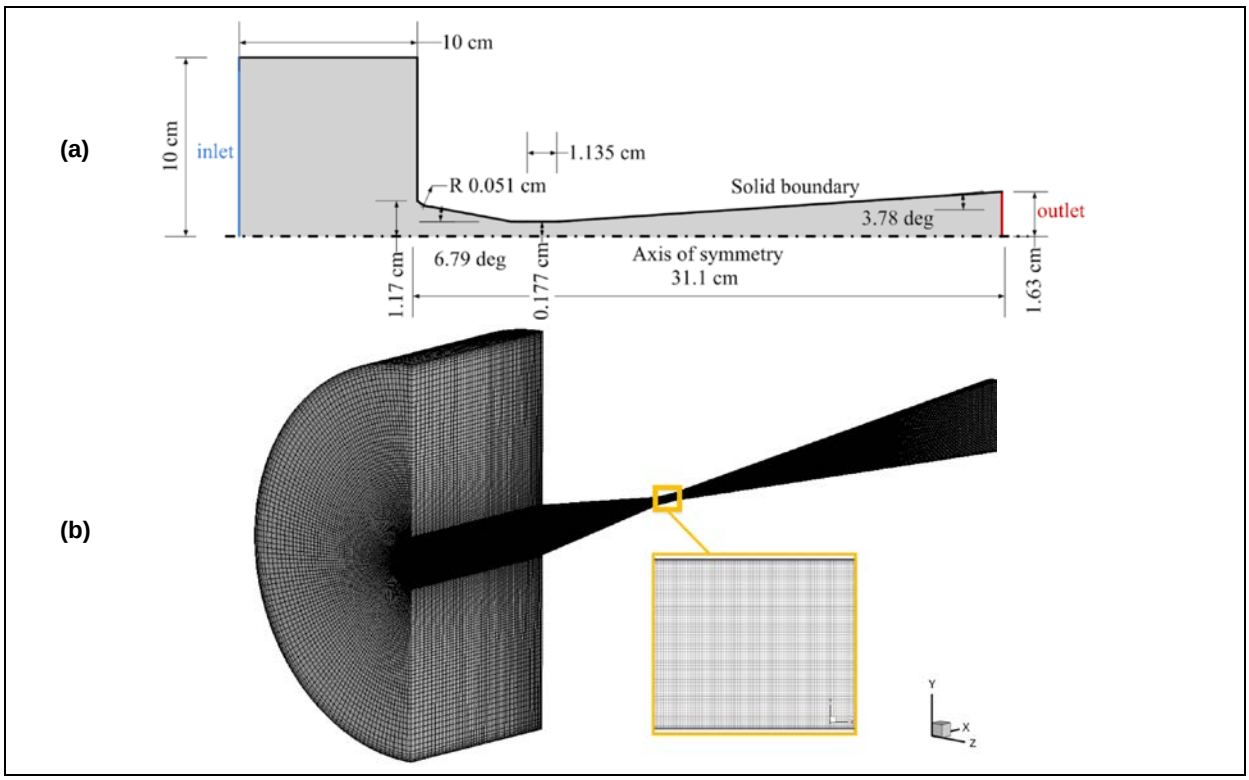

Figure 1: (a) Geometrical layout of the nozzle and (b) computational grid used in DES.

Validation and results

The pressure-based solver employing the Hertz-Knudsen vaporisation model has been extensively validated with reference to flashing internal and external flows considering water as the working medium, as reported in [17]. More specifically, the model has been demonstrated to accurately capture phase-change in a converging-diverging nozzle similar to the one in the present study, a (throttle) nozzle with an abrupt contraction and a highly-pressurized pipe.

The accuracy of the employed solver and the REFPROP database regarding the supercritical regime has been verified against the quantitative measurements of Mayer et al. [20] for a N_2 jet, since quantitative data on supercritical LOX could not be obtained from the open literature. The jet enters at a velocity of 5.4 m/s a chamber where supercritical pressure 3.98 MPa) and temperature (137 K) conditions persist. The Reynolds number characterising the injection is equal to $1.53 \cdot 10^5$. Fig. 2 depicts the average density distribution along the jet axis obtained through 3D LES, while the averaged density field is presented in the figure inset. It is demonstrated that very good agreement is achieved between numerical and experimental results.

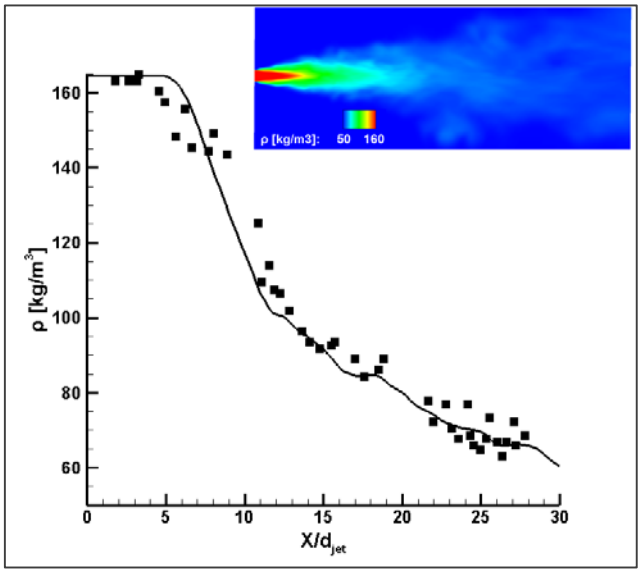

Figure 2: Comparison of numerical predictions of the average N_2 jet density distribution at the jet axis (solid line) against experimental data (symbols) [20]. The average density contour plot is depicted in the inset.

The test cases examined in this study are summarised in Table 1, along with the boundary and initial conditions for each simulation. As can be seen, both sub- and supercritical injection pressures have been considered. More specifically, the conditions of case 1 were selected to resemble the actual operating conditions prevailing in the Vulcain 2 first-stage engine of Ariane 5 [21]. Furthermore, the pressure and temperature conditions of case 2 were obtained from the experimental campaign of Hendricks et al. [4] for which data regarding the pressure distribution along the orifice are available. Finally, the pressure conditions of case 3 were specifically selected so that the pressure difference to match that of case 1. The rationale was to pinpoint the significant discrepancies in expansion dynamics between sub- and supercritical pressure injection despite the similarity in macroscopic flow parameters.

Table 1. Matrix of test cases examined. It must be noted that temperature lies in the subcritical regime in all cases.

	Case 1	Case 2	Case 3
P_{in} (=P_{init}) $\cdot 10^5$ [Pa]	133.0	11.4	43.0
$P_{out} \cdot 10^5$ [Pa]	100.0	2.6	10.0
T_{in} (=T_{init}) [K]	93.6	115.3	93.6
Pressure Regime	Supercritical	Subcritical	Subcritical
Phase-change model	REFPROP	Hertz-Knudsen, Eq. (2)	Hertz-Knudsen, Eq. (2)
u_{init} [m/s]	0.14	0.14	0.14
Walls	Adiabatic walls, No slip condition, Near-wall model for turbulence with $y^+ \approx 1$		

Fig. 3 presents the in-nozzle flow field for Case 1 lying in the supercritical pressure regime, as produced by the URANS solver. It has to be noted that the flow reaches steady-state conditions. As can be observed, the flow exhibits smooth transitions regarding all the plotted quantities. The pressure remains at supercritical levels except for the throat area, where, as expected the flow accelerates due to the geometrical constriction with a consequent pressure drop (Fig. 3a). The phase change setting in at the contracting section is moderate and accompanied by a mild temperature drop, while the fluid retains a liquid-like densities (Fig. 3b). Overall, the flow field exhibits no appreciable distinct features and abrupt gradients in the basic flow quantities were not identified.

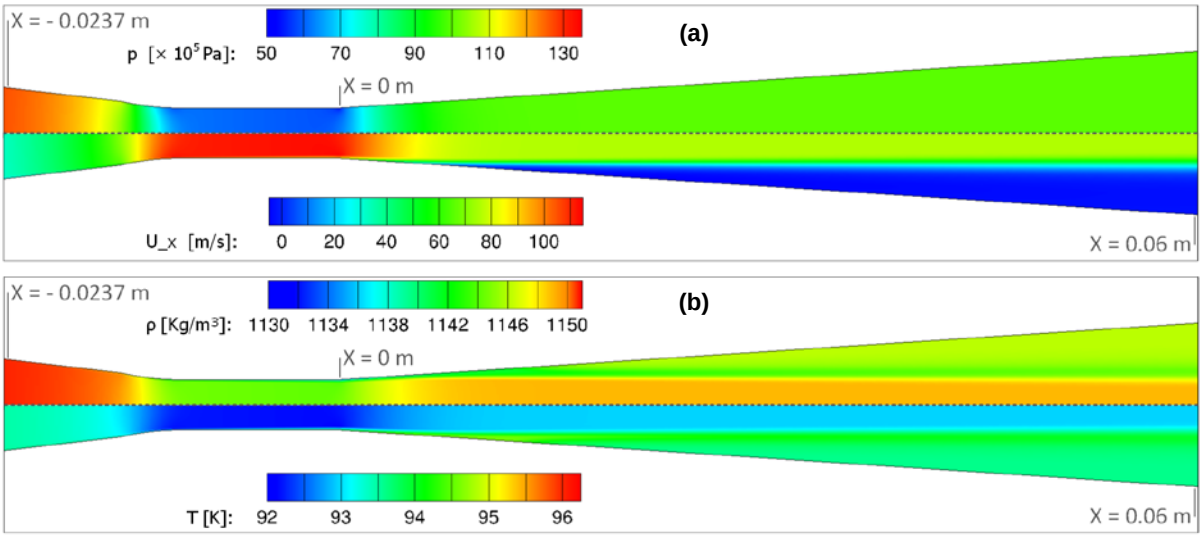

Figure 3. Contour plots of (a) pressure (upper half), axial velocity (lower half), (b) density (upper half) and temperature (lower half) for case 1 (supercritical regime) of Table 1.

Likewise, Fig. 4 presents the flow field emerging for case 2 of Table 1, as predicted by the URANS solver, where pressure lies entirely in the subcritical regime. The flow exhibits typical characteristics of an expanding flashing flow. The fluid sustains a rapid pressure drop at the contraction region, while the flow keeps accelerating in the nozzle diverging section, as well (Fig. 4a). Since, the fluid velocity in the converging nozzle part is adjusted by the local speed of sound, which in turn is much lower for the two-phase mixture compared to the pure phases, the fluid expands violently to supersonic velocities in the diverging part. The pressure re-adjusts to its outlet value through the formation of a shockwave demonstrating that the flow has reached supersonic values past the nozzle throat. Bulk vaporisation, i.e. flash boiling, sets in at the throat region and the fluid is almost fully vaporised further

downstream (Fig. 4b). Temperature drops significantly due to the conversion of sensible to latent heat during the phase change process.

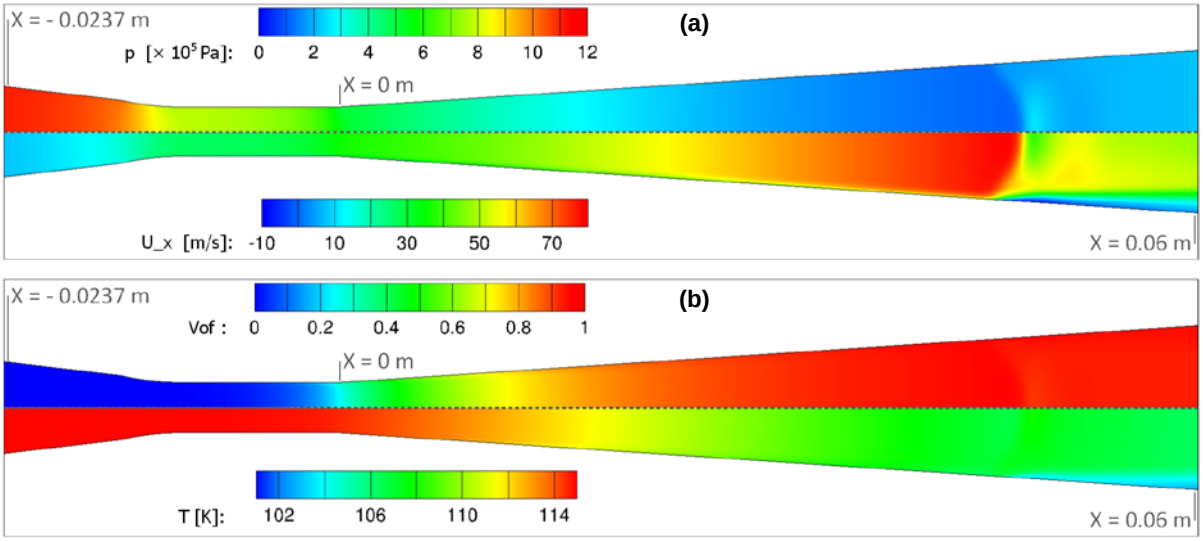

Figure 4. Contour plots of (a) pressure (upper half), axial velocity (lower half), (b) vapour volume fraction (upper half) and temperature (lower half) for case 2 (subcritical regime) of Table 1.

The pressure and volume-fraction distributions as predicted by the URANS simulations and DES are depicted in Fig. 5. It should be noted that the DES results correspond to the averaged flow field obtained through the statistics recorded for a time duration equal to five times the liquid residence time within the orifice. As can be seen in Fig. 5a, the predictions of the two numerical approaches are in concurrence with one another, as well with the available experimental data [4]. The location of the prevailing shockwave is indicative by the local maxima of the distributions. Besides, as depicted in Fig. 5b both methods predict rapid and full liquid vaporisation slightly downstream the nozzle throat (X=0).

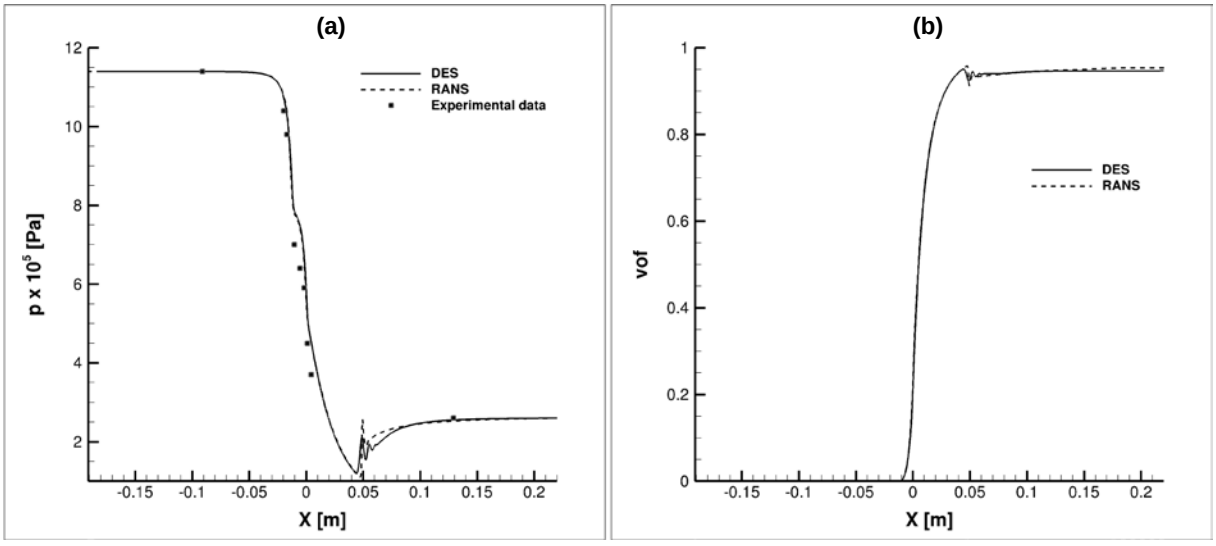

Figure 5: (a) Pressure and (b) vapour volume fraction distribution along the nozzle axis of symmetry for case 2 of Table 1.

The flow field corresponding to case 3 of Table 1, where a more severe expansion of the two-phase jet is expected compared to case 2, is depicted in Fig. 6. As shown in the pressure and velocity contour plots, the flow field bears great resemblance to that of an over-expanded gas jet [22]. As can be clearly discerned in the pressure contour plot (Fig. 6a), a series of shock diamonds emerges in the nozzle diverging geometry, followed by rarefaction waves in a typical sequence alternating between high and low-pressure regions. The Mach-disk locations of the first two shock cells, where the flow transits from supersonic to subsonic velocities, is distinctively highlighted by the presence of oblique shocks 'pointing' exactly at the disk location, while it also clearly coincides with the location where the flow exhibits an abrupt deceleration. As illustrated by Fig. 6b phase change is considerably limited compared to case 2, owing to the presence of the complex shock-wave structures pressurising the fluid to values

above the saturation pressure of oxygen. The same applies to the temperature variation which is of the order of 2 K, since it is closely connect to phase change.

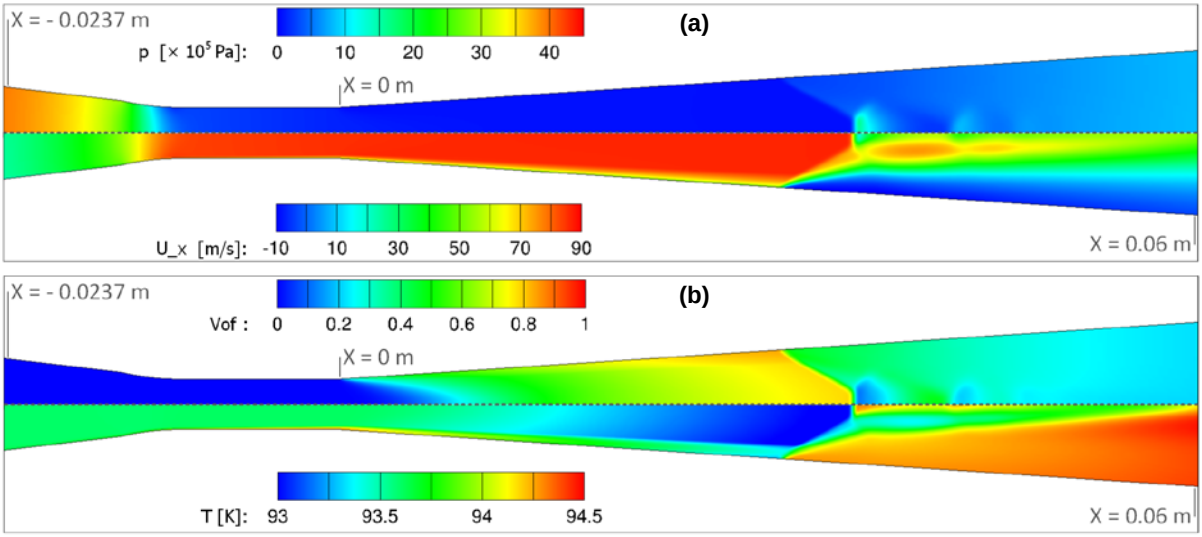

Figure 6. Contour plots of (a) pressure (upper half), axial velocity (lower half), (b) vapour volume fraction (upper half) and temperature (lower half) for case 3 (subcritical regime with an inlet-outlet pressure difference equal to that of the supercritical case 1) of Table 1.

Similar to the previous cases, Fig. 7 presents the axial distribution of pressure (Fig. 7a) and vapour volume fraction (Fig. 7b) along the orifice axis. The numerical results produced by the URANS simulations and DES are in general concurrence, yet some characteristic differences can be identified. Referring to the pressure distribution (Fig. 7a), the two approaches produce identical predictions, with the exception of the shock cell region. As can be seen, the pressure distribution obtained through the URANS simulations exhibits a clear peak corresponding to the location of the first, prevailing shockwave, which on the contrary appears much smoother in the DES results. The difference should be attributed to the effect of hydrodynamic instabilities on the average flow field. Unlike the URANS simulations were the flow reaches steady conditions, the DES results predict certain transient effects, in the sense that the emerging shock waves do not remain completely static. Hence, averaging of the pressure field leads to observed smoothing in the shockwave location. The topology of hydrodynamic instabilities, as predicted by DES will be further elucidated in the next section.

Likewise, as depicted in Fig. 7b, the vapour volume fraction gradients predicted by the URANS simulations are steeper to the respective predicted by DES. Once again, the differences should be attributed to hydrodynamic effects, as the DES predicts a transient flapping of the accelerating fluid core in the divergent nozzle region (as also depicted in Fig. 8), i.e. its position deviates from the symmetry axis. Hence, this transient behaviour affects the vaporisation process, unlike the URANS simulations where the accelerating core always remains steady at the nozzle axis.

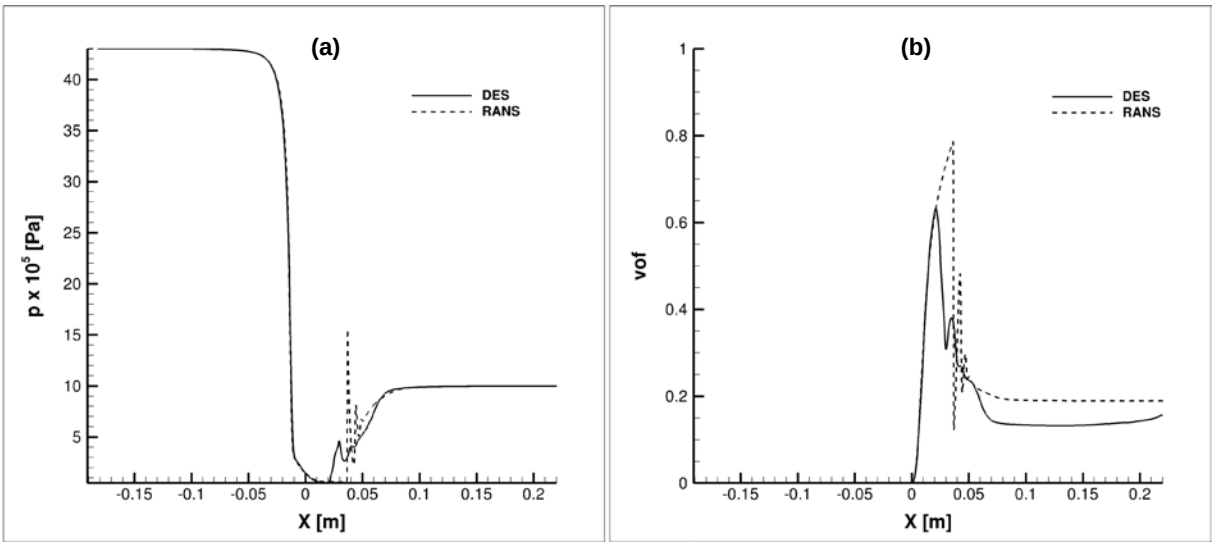

Figure 7: (a) Pressure and (b) vapour volume fraction distribution along the nozzle axis of symmetry for case 3 of Table 1.

Hydrodynamic instabilities

The elucidation of the influence of hydrodynamic instabilities is of high practical importance, since they can affect the delivery performance of the oxidiser injector with subsequent consequences on the combustion efficiency. Fig. 8 depicts three characteristic DES time instances for the subcritical case 2 of Table 1, where a severe jet expansion has been observed. A detailed view of the region slightly downstream the nozzle throat is depicted, while half of the nozzle cross-section is included to enhance the clarity of the figure. The black line evident on the vectors-over-contour plots signifies regions where M=1.The three instance make clear that the flow is oriented to the direction of the oblique shock-waves and remains parallel in the region encompassed by the M=1 iso-line. On the contrary, as depicted in all three instances a complex recirculation pattern sets in at the subsonic boundary layer. It is also interesting to notice in Figs 8a and 8c that the flow turns away from the nozzle axis, i.e. towards the wall in the flow regions in the vicinity of Mach disks (annotated as regions 1-3 in the plots). This flow behaviour is also similar to the velocity field of expanding supersonic gas jets. Finally, as shown in Fig. 8b (region 4) significant flow deceleration and transition to the subcritical regime perturbs the flow significantly, so as to induce the emergence of an extensive recirculation pattern even at the channel core, where parallel flow prevails in the other time instances.

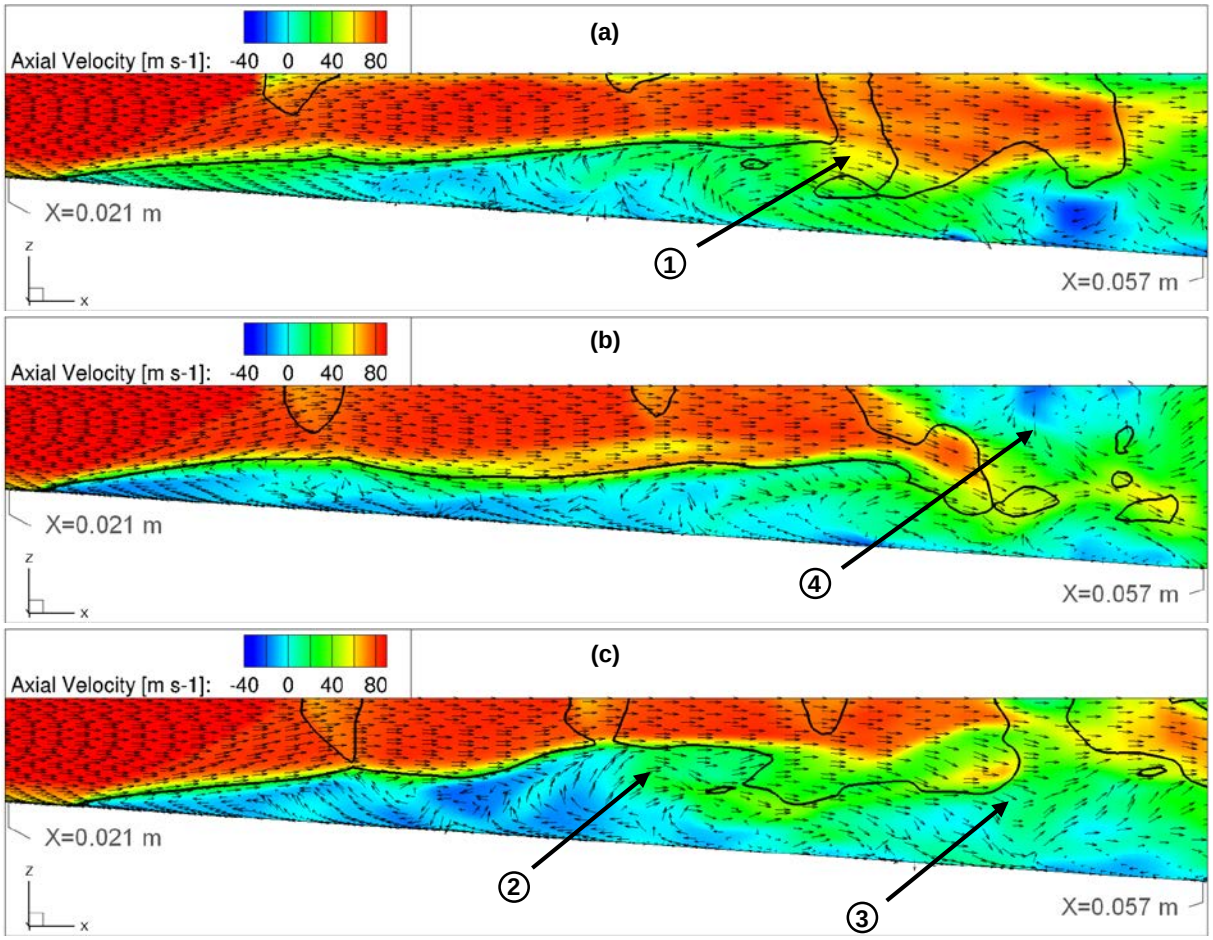

Figure 8: Axial velocity contour plots and velocity vectors in a detailed view of the nozzle diverging part corresponding to characteristic time instances of DES: (a) t, (b) t+1.0 ms and (c) t+2.0 ms. The black iso-line signifies M=1 regions, while the numbered vectors indicate regions of distinct flow features.

Conclusions

Two-phase oxygen flow was numerically investigated in a converging diverging nozzle in both sub- and supercritical pressure conditions using URANS simulations and DES. It has been demonstrated that the phase-change process can be accurately captured employing a Hertz Knudsen equation in the subcritical regime and the REFPROP look-up table with regard to supercritical injection. Hence, a complete numerical methodology for the entire range of conditions that can be met with relevance to LOX injection for rocket applications has been established. From a flow physics standpoint, in the supercritical regime the flow exhibits smooth transitions for all quantities of interest. Overall, the flow field exhibits no appreciable distinct features and abrupt gradients. On the contrary, in the subcritical regime, flash boiling of LOX takes place, i.e. abrupt vaporisation of the liquid phase, accompanied by flow acceleration to supersonic velocities and abrupt pressure gradients. In the case, with the most severe two-phase jet expansion examined in this study, a series of shock-diamonds set in at the nozzle diverging region verifying the flow similarity to the expansion of a supersonic gas jet. DES demonstrated that the flow transition from

the super- to the subsonic regime perturbs the velocity field and gives rise to extensive recirculation patterns both in the boundary-layer region, as well as in the channel core in the vicinity of the Mach disk's locations. The main findings of this study are applicable to propulsion components of space vehicles where LOX is currently the prevalent oxidiser option but also to other applications where cryogenic liquids are the working media, e.g. CO_2 for refrigeration systems.

Acknowledgements

This investigation has received funding from the European Union Horizon 2020 Research and Innovation programme HAOS (Grant No. 675676) and the Marie Skłodowska-Curie Actions Global Fellowships AHEAD (Grant No. 794831) and UNIFIED (Grant No. 748784).

Nomenclature

a	volume fraction [-]
A	area [m^2]
d	diameter [m]
L	characteristic length [m]
M	Mach number [-]
p	pressure [Pa]
Re	Reynolds Number [-]
R_g	specific gas constant [J/kgK]
T	temperature [K]
t	time [s]
u	velocity [m/s]

Greek Letters

λ	accommodation coefficient [-]
λ_g	Taylor length scale [m]
μ	dynamic viscosity [kg/ms]
ρ	density [kg/m^3]

Subscripts

in	inlet
init	initial
int	interface
out	outlet
sat	saturation
v	vapour

References

[1] Harstad, K., Bellan, J.,1998, International journal of heat and mass transfer, 41 (22), 3551-3558.
[2] Meng, H., Yang V.,2014, International Journal of Heat and Mass Transfer 68, 500–508.
[3] HABIBALLAH*, M., Orain, M., Grisch, F., Vingert, L., Gicquel, P., 2006, Combustion Science and Technology, 178 (1-3), 101-128.
[4] Hendricks, R.C., Simoneau, R.J., Barrows, R.F., 1976, NASA Technical Note.
[5] Mayer, W., Tamura, H., 1996, Journal of Propulsion and Power, 12 (6), 1137-1147.
[6] Mayer, H.W.O., Schik, A.H.A., Vielle, B., Chauveau, C., Goekalp, I., Talley, D.G., Woodward, R.D., 1998, Journal of Propulsion and Power, 14 (5), 835-842.
[7] Chehroudi, B., Talley, D., Coy, E., 2002, Physics of Fluids, 14 (2), 850-861.
[8] Lamanna, G., Kamoun, H., Weigand, B., Manfletti, C., Rees, A., Sender, J., Oschwald, M., Steelant, J., 2015, Atomization and Sprays, 25 (10).
[9] Zong, N., Yang, V., 2008, Physics of Fluids, 20 (5).
[10] Wang, X., Huo, H., Wang, Y., Zhang, L., Yang, V., 2015, 53rd AIAA Aerospace Sciences Meeting, p1827.
[11] Wang, X., Huo, H., Wang, Y., & Yang, V., 2017, AIAA Journal, 3109-3119.
[12] Sher, E., Bar-Kohany, T., Rashkovan, A., 2008, Progress in energy and comb. science, 34 (4), 417-439.
[13] Travis, J.R., Koch, D.P., Breitung, W., 2012, Int. J. of hydrogen energy, 37 (22), 17373-17379.
[14] Lyras, K., Dembele, S., Schmidt, D.P., Wen, J.X., 2018, Int. J. of Multiphase Flow, 102, 16-28.
[15] Schmehl, R., Steelant, J., 2009, Journal of Propulsion and Power, 25 (3), 771-782.
[16] Ramcke, T., Lampmann, A., Pfitzner, M., 2018, Journal of Propulsion and Power, 34 (2), 395-407.
[17] Karathanassis, I. K., Koukouvinis, P., and Gavaises, M., 2017, Int. J. Multiph. Flow, 95, 257–270.
[18] Schmidt, R., Wagner, W., 1985, Fluid Phase Equilibria, 19, 175-200.
[19] Lemmon, E. W., Jacobsen, R. T., 2004, International Journal of Thermophysics, 25 (1).
[20] Mayer, W., Telaar, J., Branam, R., Schneider, G., and Hussong, J., 2003, Heat Mass Transf., 39 (8–9), 709–719.
[21] http://www.arianespace.com/vehicle/ariane-5/
[22] Edgington-Mitchell, D., Honnery, D. R., Soria, J., 2014, Phys. Fluids, 26 (9).